# Dynamic shadow of a black hole with a self-interacting massive complex scalar hair\*

Mingzhi Wang (王明智)<sup>1†</sup> Cheng-Yong Zhang (张承勇)<sup>2‡</sup> Songbai Chen (陈松柏)<sup>3,4‡</sup> Jiliang Jing (荆继良)<sup>3,4‡</sup>

School of Mathematics and Physics, Qingdao University of Science and Technology, Qingdao, Shandong 266061, People's Republic of China
 College of Physics and Optoelectronic Engineering, Jinan University, Guangzhou 510632, People's Republic of China
 Institute of Physics and Department of Physics, Key Laboratory of Low Dimensional Quantum Structures and Quantum Control of Ministry of Education, Synergetic Innovation Center for Quantum Effects and Applications, Hunan Normal University, Changsha, Hunan 410081, People's Republic of China

<sup>4</sup>Center for Gravitation and Cosmology, College of Physical Science and Technology, Yangzhou University, Yangzhou 225009, People's Republic of China

Abstract: We research dynamic shadows of a black hole with a self-interacting massive complex scalar hair. The complex scalar field  $\psi$  evolves with time t, whose magnitude on apparent horizon  $|\psi_b|$  starts from zero, undergoes a sharp rise followed by rapid oscillations, and eventually converges to a constant value. The variation of the photon sphere radius  $r_{ps}$  is similar to that of the magnitude  $|\psi_h|$ . The emergence of the complex scalar hair  $\psi$  causes the apparent horizon radius  $r_h$  to start increasing sharply, and smoothly approaches a stable value eventually. The shadow radius  $R_{sh}$  of the black hole with an accretion disk increases with  $t_o$  the time at the observer's position. In the absence of an accretion disk, the shadow radius  $R_{sh}$  is larger and also increases as  $t_o$  increases. Furthermore, we slice the dynamical spacetime into spacelike hypersurfaces for all time points t. For the case with an accretion disk, the variation of  $R_{sh}$  is similar to that of the apparent horizon  $r_h$ , because the inner edge of the accretion disk extends to the apparent horizon. In the absence of an accretion disk, the variation of  $R_{sh}$  is similar to that of the photon sphere  $r_{ps}$ , because the black hole shadow boundary is determined by the photon sphere. Since the variation of  $r_{ps}$  is induced by  $\psi$ , it can be stated that the variation in the size of the shadow is likewise caused by the change of  $\psi$ . Regardless of the presence or absence of the accretion disk, the emergence of the complex scalar hair  $\psi$  causes the radius  $R_{sh}$  of the shadow to start changing. Moreover, we investigate the time delay  $\Delta t$  of lights propagating from light sources to observer. These findings not only enrich the theoretical models of dynamic black hole shadows but also provide a foundation for testing black hole spacetime dynamics.

Keywords: black hole shadow, dynamic shadow, accretion disk, photon sphere

DOI: CSTR:

### I. INTRODUCTION

The images of supermassive black holes at the center of the giant elliptical galaxy M87 and the Milky Way galaxy has been published by the Event Horizon Telescope (EHT) Collaboration [1, 2]. It not only confirms the existence of black holes in our universe but also marks a milestone in the fields of astrophysics and black hole physics. An increasing number of scholars have begun to focus on the study of black hole images. The black hole shadow [3–6] is the dark silhouette in a black hole image.

It appears because photons close to the black hole can be absorbed or bent, leaving a dark shadow in the observer's sky. Analyzing the characteristics of black hole images can reveal the spacetime structure of black holes, the dynamics of accretion disks, and the physical laws in strong gravitational fields. Nowadays, a large amount of research on black hole images focuses on constraining black hole parameters [7–13], investigating dark matter [14–18], and verifying various theories of gravity [19–32]. Many other aspects of black hole shadows have been studied in Refs.[33–57].

Received 3 August 2025; Accepted 17 October 2025

<sup>\*</sup> This work was supported by the National Natural Science Foundation of China under Grant No. 12105151, the Shandong Provincial Natural Science Foundation of China under Grant No. ZR2020QA080, and was partially supported by the National Natural Science Foundation of China under Grant No. 12375048, 11875026, 11875025 and 12035005

<sup>†</sup> E-mail: wmz9085@126.com

<sup>‡</sup> E-mail: zhangcy@email.jnu.edu.cn

<sup>§</sup> E-mail: csb3752@hunnu.edu.cn

<sup>&</sup>lt;sup>‡</sup> E-mail: jljing@hunnu.edu.cn

<sup>©2025</sup> Chinese Physical Society and the Institute of High Energy Physics of the Chinese Academy of Sciences and the Institute of Modern Physics of the Chinese Academy of Sciences and IOP Publishing Ltd. All rights, including for text and data mining, AI training, and similar technologies, are reserved.

Most research on black hole images only considers static or stationary black holes. The collapse of a compact star into a black hole, perturbation of a black hole, or mergers of black holes all result in dynamic spacetime. Research on black hole images in dynamical spacetime is extremely scarce, yet these dynamic images hold significant significance for the study of black holes and gravitational theories. Currently, the EHT team is working on creating a movie for Sgr A\* because of its rapidly changing appearance, hoping to understand the black hole's structure. We have investigated the dynamic shadows of a Schwarzschild black hole perturbed by a specific polar gravitational wave[33], and demonstrated that the black hole shadow exhibits periodic variations, oscillating in response to the gravitational wave's perturbation. Y. P. Zhang et al have investigated the dynamic emergence of black hole shadows in the spacetime of a collapsing boson star[58], revealing the evolutionary behaviors of Einstein rings and the distinct formation processes of shad-

In this paper, we study the shadows of a black hole with a self-interacting massive complex scalar hair. The nonlinear self-interaction can induce black hole bomb phenomena beyond the famous superradiant instability[59]. It will make the spacetime dynamic, causing the black hole shadow to change over time. The dynamic black hole shadows can serve as a powerful tool for studying the dynamical evolution of black hole spacetime. With the next generation Event Horizon Telescope(ngEHT), future astronomical observations could potentially capture dynamic black hole images, offering unprecedented insights into their temporal evolu-

The paper is organized as follows. In Section II, we first briefly introduce the dynamical spacetime of a black hole with a self-interacting massive complex scalar hair. Then we calculate the photon sphere radius  $r_{ps}$ , and study how  $r_{ps}$  evolves with time t under the effect of the complex scalar field  $\psi$ . In Section III, we present the specific intensity of the direct, lensing and photon ring emission of a faced-on thin disk in the dynamical spacetime. With or without an accretion disk, the variations of the black hole shadow radius  $R_{sh}$  with the observer's time  $t_o$  and with the coordinate time t are investigated. Moreover, we study the time delay  $\Delta t = t_o - t_e$  of lights propagating from light sources to observer in the dynamical spacetime. Finally, we present a conclusion. In this paper, we employ the geometric units G = c = M = 1.

# II. THE DYNAMICAL SPACETIME OF A BLACK HOLE WITH A SELF-INTERACTING MASSIVE COMPLEX SCALAR HAIR

The black hole spacetime we consider is the Einstein-

Maxwell gravity minimally coupled with a self-interacting massive complex scalar  $\psi[59]$ . The Lagrangian density is

$$\mathcal{L} = R - F_{\mu\nu}F^{\mu\nu} - D^{\mu}\psi(D\psi)^* - V(\psi). \tag{1}$$

 $F_{\mu\nu} = \partial_{\mu}A_{\nu} - \partial_{\nu}A_{\mu}$  is the Maxwell field strength with  $A_{\mu}$  is the gauge potential. The gauge covariant derivative is defined as  $D_{\mu} = \nabla_{\mu} - iqA_{\mu}$ , where q denotes the gauge coupling constant of the complex scalar field  $\psi$ . The potential is given by  $V(\psi) = \mu^2 |\psi|^2 - \lambda |\psi|^4 + \nu |\psi|^6$ , with  $\mu$  as the scalar field mass, and  $\lambda, \nu$  as positive self-interaction parameters[59]. The Einstein equations are given as

$$R_{\mu\nu} - \frac{1}{2}g_{\mu\nu}R = 2T^{A}_{\mu\nu} + T^{\psi}_{\mu\nu},\tag{2}$$

where the energy-momentum tensors are

$$T_{\mu\nu}^{A} = F_{\mu\rho}F_{\nu}^{\rho} - \frac{1}{4}g_{\mu\nu}F_{\rho\sigma}F^{\rho\sigma}, \tag{3}$$

$$T^{\psi}_{\mu\nu} = \frac{1}{2} (D_{\mu}\psi)^* (D_{\nu}\psi) + \frac{1}{2} (D_{\mu}\psi) (D_{\nu}\psi)^* + \frac{1}{2} g_{\mu\nu} (D^{\mu}\psi (D_{\mu}\psi)^* + V).$$
 (4)

The Maxwell equations are written as

$$\nabla_{\mu}F^{\mu\nu} = \frac{1}{4}iq[\psi^*\nabla_{\mu}\psi - \psi(\nabla_{\mu}\psi)^*]g^{\mu\nu}.$$
 (5)

The scalar equation is written as

$$D^{\mu}D_{\mu}\psi = \frac{\partial V}{\partial |\psi|^2}\psi. \tag{6}$$

The dynamic black hole with the self-interacting massive complex scalar hair in the Painlev $\acute{e}$ -Gullstrand (PG) coordinates is described as follows:

$$ds^{2} = -[1 - \zeta(t, r)^{2}]\alpha(t, r)^{2}dt^{2} + 2\alpha(t, r)\zeta(t, r)dtdr + dr^{2} + r^{2}(d\theta^{2} + \sin^{2}\theta d\phi^{2}).$$
 (7)

Here  $\alpha, \zeta$  are metric functions dependent on t and r. This coordinate system remains regular at the apparent horizon  $r_h$  where  $\zeta(t, r_h) = 1$ . The gauge potential  $A_{\mu}dx^{\mu} = Adt$ . Introducing auxiliary variables [59]

$$\Phi = \partial_r \psi, \tag{8}$$

$$\Pi = \frac{1}{\alpha} (\partial_t \psi - iqA\psi) - \zeta \Phi, \tag{9}$$

$$B = -\frac{1}{\alpha} \partial_r A. \tag{10}$$

The Einstein equations can be reduced to

$$0 = \partial_r \alpha + \frac{\alpha r \operatorname{Re}(\Pi \Phi^*)}{2\zeta},\tag{11}$$

$$0 = \partial_r \zeta + \frac{\zeta}{2r} - \frac{r}{4\zeta} (\Pi \Pi^* + \Phi \Phi^* + 2B^2 + V) - \frac{r}{2} \operatorname{Re}(\Pi \Phi^*),$$
(12)

$$0 = \partial_t \zeta - \frac{1}{2} \alpha r \left[ \Pi \Pi^* + \Phi \Phi^* + \left( \zeta + \frac{1}{\zeta} \right) \operatorname{Re}(\Pi \Phi^*) \right]. \tag{13}$$

The Maxwell equations are give as

$$0 = \partial_r B + \frac{2B}{r} - \frac{q}{2} \operatorname{Im}(\Pi \Phi^*), \tag{14}$$

$$0 = \partial_t B - \frac{q}{2} \alpha \operatorname{Im}[(\zeta \Pi + \Phi) \psi^*]. \tag{15}$$

The scalar equation becomes

$$0 = \partial_t \Pi - \partial_r [\alpha(\Pi \zeta + \Phi)] - \frac{2\alpha(\Pi \zeta + \Phi)}{r} - iA\Pi q + \alpha \psi \frac{\partial V}{\partial |\psi|^2}.$$
(16)

At asymptotic spatial infinity, there are

$$\zeta = \sqrt{\frac{2M}{r} \left[ 1 + O\left(\frac{1}{r}\right) \right]},\tag{17}$$

where M is the total mass. By numerically solving the above equations, we can obtain the complex scalar field  $\psi(t,r)$ , the gauge potential A(t,r), and metric  $\{\alpha(t,r),\zeta(t,r)\}$  over all positions (r) and all times (t). In this paper, we set the potential  $V(\psi) = |\psi|^2 (1 - \frac{|\psi|^2}{0.1^2})^2$ , M = 1.09239, the total charge Q = 0.9, and Q = 3.

Figure 1 illustrates the contour plot of the metric component  $g_{tt}$  as functions of time t and radial coordinate r. The contour line of  $g_{tt} = 0$  corresponds to the location of the apparent horizon  $r_h$ , which increases with time t. The  $g_{tt}$  has little variation with t and asymptotically approaches -1 as r tends to infinity. Figure 2 displays a contour plot of  $g_{tr}$  as a function of t and r. The  $g_{tr}$  also

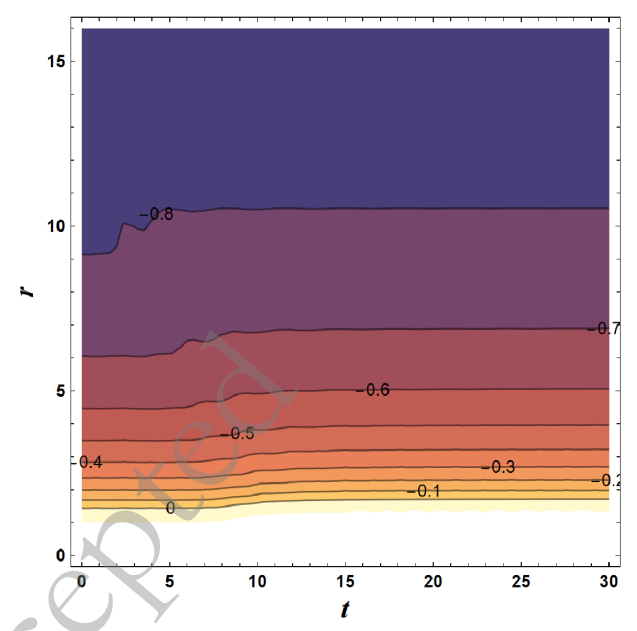


**Fig. 1.** (color online) The contour plot of  $g_{tt}$  as a function of time t and radial coordinate r, which asymptotically approaches -1 as  $r \to \infty$ . The contour line of  $g_{tt} = 0$  corresponds to the position of apparent horizon  $r_h$ .

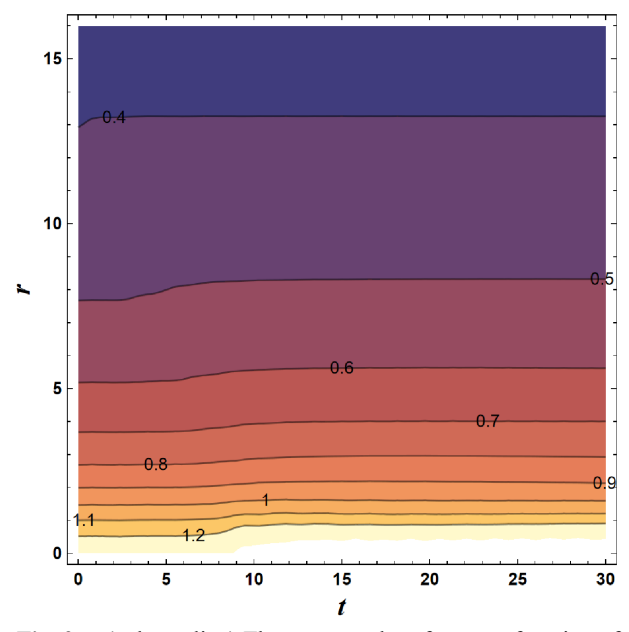


**Fig. 2.** (color online) The contour plot of  $g_{tr}$  as a function of time t and radial coordinate r, which asymptotically approaches 0 as  $r \to \infty$ .

has little variation with t and asymptotically approaches 0 as r tends to infinity. The metric of this dynamic black hole describes an asymptotically flat spacetime. The complex scalar field  $\psi(t,r)$  of this black hole is a function of t and r. Figure 3 depicts how the magnitude of the complex scalar field on the horizon  $|\psi_h|$  changes over time. Initially,  $|\psi_h| = 0$ , and at this point, the black hole has not

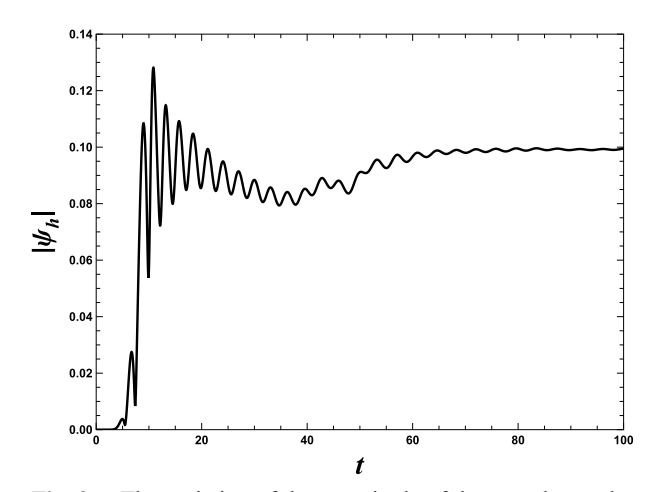


**Fig. 3.** The variation of the magnitude of the complex scalar field on the horizon  $|\psi_h|$  with time t.

yet acquired scalar hair. Then there is a sharp rise followed by rapid oscillations. As time progresses, the oscillation gradually dampen, and then the magnitude tends toward stabilization.

The Lagrangian  $\mathcal{L}$  of a photon propagation in the spacetime can be characterized by

$$\mathcal{L} = \frac{1}{2} g_{\mu\nu} \dot{x}^{\mu} \dot{x}^{\nu} = \frac{1}{2} [-(1 - \zeta^2)\alpha^2 \dot{t}^2 + 2\alpha \zeta \dot{t}\dot{r} + \dot{r}^2 + r^2 (\dot{\theta}^2 + \sin^2 \theta \dot{\phi}^2)] = 0.$$
 (18)

Since the variable  $\phi$  is not present in  $\mathcal{L}$ ,  $p_{\phi}$  is a conserved quantity in the motions of photons, and can be depressed as angular momentum

$$L = p_{\phi} = \frac{\partial \mathcal{L}}{\partial \dot{\phi}} = r^2 \sin^2 \theta \dot{\phi}. \tag{19}$$

Since the spacetime is spherically symmetric, without any loss of generality, we investigate the photon motion in the plane  $\theta = \pi/2$ . The Lagrangian  $\mathcal{L}(18)$  can be rewrote as

$$\mathcal{L} = \frac{1}{2} [-(1 - \zeta^2)\alpha^2 \dot{t}^2 + 2\alpha \zeta \dot{t} \dot{r} + \dot{r}^2 + r^2 \dot{\phi}^2] = 0. \tag{20}$$

The photon sphere is closely associated with the shadows of black holes, satisfying

$$\dot{r} = 0 \quad and \quad \ddot{r} = 0, \tag{21}$$

where the dot  $\cdot$  denotes the derivative with respect to the affine parameter. According to  $\mathcal{L} = 0(20)$  and  $\dot{r} = 0$ , one can obtain

$$-(1-\zeta^2)\alpha^2 \dot{t}^2 + r^2 \dot{\phi}^2 = -(1-\zeta^2)\alpha^2 \dot{t}^2 + \frac{L^2}{r^2} = 0.$$
 (22)

The equations of geodesic motion in this spacetime are

$$\ddot{t} = -\left(\frac{1}{2}g^{tt}g_{tt,t} + \frac{1}{2}g^{tr}\left(2g_{tr,t} - g_{tt,r}\right)\right)\dot{t}^{2} - g^{tt}g_{tt,r}\dot{t}\dot{r}$$
$$-g^{tt}g_{tr,r}\dot{r}^{2} + g^{tr}r\dot{\theta}^{2} + g^{tr}\frac{L^{2}}{r^{3}\sin^{2}\theta},$$
(23)

$$\ddot{r} = -\left(\frac{1}{2}g^{tr}g_{n,t} + g_{tr,t} - \frac{1}{2}g_{n,r}\right)\dot{t}^2 - g^{tr}g_{n,r}\dot{t}\dot{r} - g^{tr}g_{tr,r}\dot{r}^2 + r\dot{\theta}^2 + \frac{L^2}{r^3\sin^2\theta},$$
(24)

$$\ddot{\theta} = \frac{L^2 \cos \theta}{r^4 \sin^3 \theta} - 2\frac{1}{r} \dot{r} \dot{\theta},\tag{25}$$

$$\dot{\phi} = \frac{L}{r^2 \sin^2 \theta}.\tag{26}$$

The radius of the photon sphere  $r_{ps}$  can be determined by solving the combined conditions derived from Eqs. (21), (22), and (24), which require that  $r_{ps}$  satisfies

$$g^{tr}g_{tt,t} + 2g_{tr,t} - g_{tt,r} + \frac{1}{r}g_{tt} = 0. (27)$$

Figure 4 illustrates the variations of photon sphere radius  $r_{ps}$  (marked by a red solid line) and the apparent horizon radius  $r_h$  (marked by a black dashed line) with respect to time t. The radius of the photon sphere  $r_{ps}$  remains constant initially, then experiences a significant and rapid increase subsequently, followed by some fluctuations, and finally stabilizes. The photon sphere radius  $r_{ps}$  exhibits a striking similarity to that of the magnitude  $|\psi_h|$  as illustrated in Fig. 3. It can be stated that the complex scalar field  $\psi$  is capable of inducing variation in the photon sphere radius  $r_{ps}$ . Moreover, it will give rise to a dynamically evolving black hole shadow and endow it with new features. The radius of the apparent horizon  $r_h$ also remains constant initially, then increases rapidly, and smoothly approaches a stable value eventually. It can be stated that the appearance of the complex scalar hair  $\psi$ causes the increase of the apparent horizon  $r_h$ .

# III. THE DYNAMIC SHADOWS OF A BLACK HOLE WITH A SELF-INTERACTING MASSIVE COMPLEX SCALAR HAIR

In this section, we calculate the shadows of the black hole with a self-interacting massive complex scalar hair by the backward ray-tracing method[4, 22, 33–47]. The light rays are assumed to evolve backward in time from

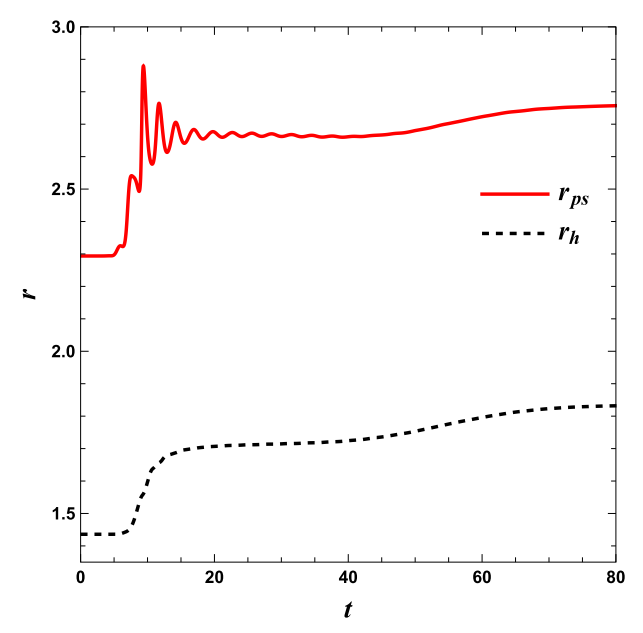


**Fig. 4.** (color online) The variations of apparent horizon  $r_h$  (marked by a black dashed line) and photon sphere  $r_{ps}$  (marked by a red solid line) with respect to the variable t.

the observer. For this purpose, it is necessary to solve the null geodesic equations numerically (23-26). Figure 5 depicts the light rays from the observer to the vicinity of the black hole. The black disk represents the black hole, and the observer is positioned to its right at a distance of  $r_0 = 50$ . The initial time for the reverse evolution of light rays at the position of the observer is  $t_0 = 170$ . We consider an optically and geometrically thin accretion disk, facing directly towards the observer. Due to the dynamical spacetime, we only consider the accretion disk extending to horizon. In this figure, the black light rays directly evolve into the black hole, according to the black hole shadow. It can be observed that the size of black hole shadow depends on the inner edge of the accretion disk. The blue rays cross the equatorial plane at most once, corresponding to direct emission; the orange rays cross the equatorial plane twice, corresponding to lensing rings; the red rays cross the equatorial plane at least three times, corresponding to photon rings[60, 61]. The total number of orbits is defined as  $n = \phi/2\pi [60, 61]$ . Figure 6(a) shows the variation of total number n with angular momentum L. In which black hole shadow satisfies the condition n < 1/4 (black); the direct emission satisfies  $1/4 \le n < 3/4$ (blue); the lensing ring satisfies  $3/4 \le n < 5/4$  (orange); the photon ring satisfies  $n \ge 5/4$ (red). Figure 6(b) exhibits the transfer functions  $r_m(L)$  for the direct emission, the lensing ring and the photon ring. The blue rays, orange rays and red rays represent the radial coordinate of the first (m = 1), second (m = 2), and third (m = 3) intersections with the thin disk, respectively.

In the spacetime of the dynamic black hole with a self-interacting massive complex scalar hair, we consider

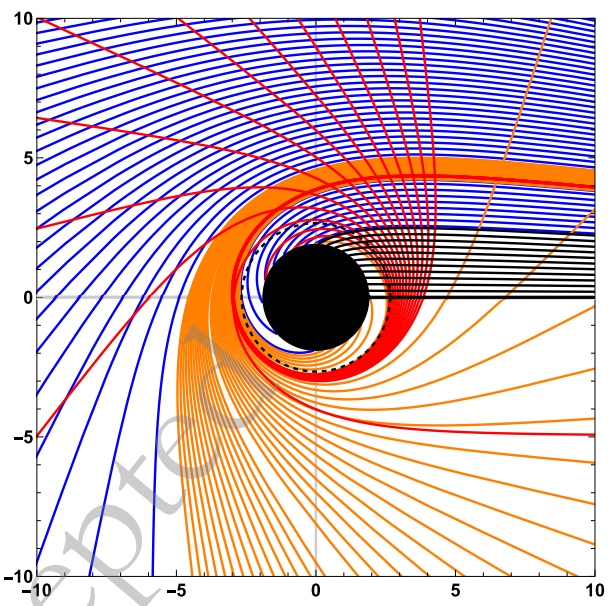


**Fig. 5.** (color online) The light rays correspond to shadow (black), direct emission (blue), lensing rings (orange), and photon rings (red). The black disk represents the black hole, and the observer is positioned to its right at a distance of  $r_o = 50$ . The accretion disk is viewed face-on by the observer.

the geometrically and optically thin accretion disk extends to horizon, and the emitted specific intensity as

$$I_{\text{em}}(t,r) = \begin{cases} I_0 \frac{\frac{\pi}{2} - \tan^{-1}(r-5)}{\frac{\pi}{2} - \tan^{-1}[r_{\text{h}}(t) - 5]}, & r > r_{\text{h}} \\ 0, & r \le r_{\text{h}}. \end{cases}$$
(28)

The emitted specific intensity  $I_{em}(t,r)$  changes over time due to the changing apparent horizon radius  $r_h(t)$ , as shown in Eq.(28). Since the accretion disk extends to the horizon, the inner radius of the accretion disk increases over time as the apparent horizon radius  $r_h(t)$  increases, as shown in Fig. 7. Moreover, the specific intensity received by the observer is

$$I_{\text{obs}} = \sum_{m} g^4 I_{em}|_{r=r_m},$$
 (29)

where  $r_m$  is the radial coordinate of the  $m^{th}$  intersection with the accretion disk plane[61]. And  $g = v_o/v_e$  is the redshift factor;  $v_e$  is the photon frequency as measured in the rest-frame of the emitter;  $v_o$  is observed photon frequency. In this dynamical spacetime, the redshift factor g can be rewrote as

$$g = \frac{v_o}{v_e} = \frac{p_\mu u_o^\mu}{p_\nu u_e^\nu},$$
 (30)

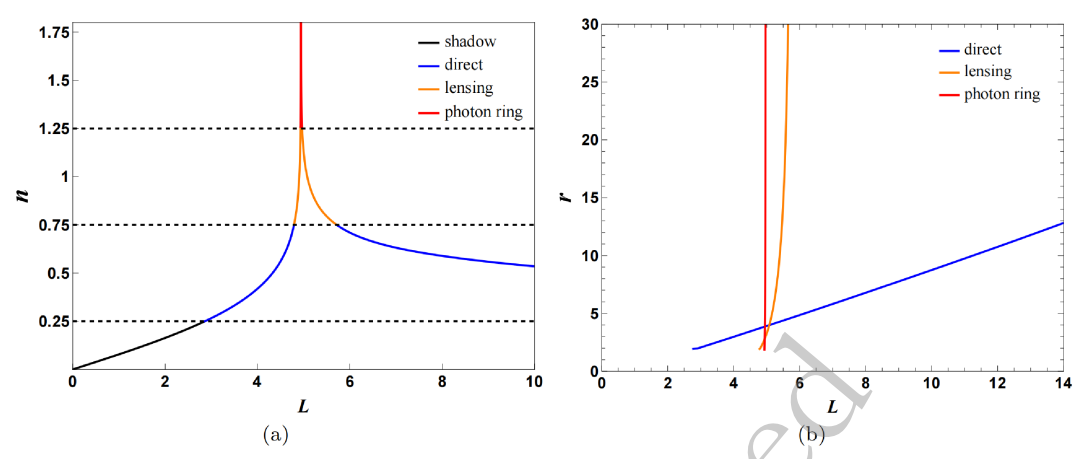
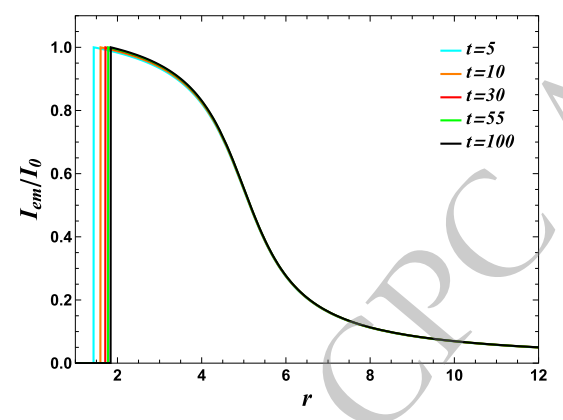


Fig. 6. (color online) (a) The variation of total number n with angular momentum L. Black hole shadow satisfies the condition n < 1/4 (black); the direct emission satisfies  $1/4 \le n < 3/4$  (blue); the lensing ring satisfies  $3/4 \le n < 5/4$  (orange); the photon ring satisfies  $n \ge 5/4$  (red). (b) The transfer functions  $r_m(L)$  for the direct emission, the lensing ring and the photon ring. The blue rays, orange rays and red rays represent the radial coordinate of the first (m = 1), second (m = 2), and third (m = 3) intersections with the thin disk, respectively.



**Fig. 7.** (color online) The variation of emitted specific intensity  $I_{em}(t,r)$  at different times t as a function of radial coordinate r.

where  $p_{\mu}$  is the 4-momentum of the photon,  $u_o^{\mu} = (1/\sqrt{-g_{tt}|_{(t_o,r_o)}},0,0,0)$  is the 4-velocity of the static observer, while  $u_e^{\mu} = (1/\sqrt{-g_{tt}|_{(t_e,r_e)}},0,0,0)$  is the 4-velocity of the accreting gas emitting the radiation. Figure 8 shows the observational appearance of the accretion disk, which viewed from a face-on by the observer with radius  $r_o = 50$  and time  $t_o = 170$ . In other words, this is the image of the black hole captured by the observer at the local time  $t_o = 170$ . Figure 8 (a) and (b) exhibit the profiles of observed intensity  $I_{obs}$  as a function of the angular momentum L and radial coordinate  $R = \sqrt{x^2 + y^2}$  in observer's sky, respectively. Here (x,y) are the celestial coordinates. Figure 8 (c) exhibits the density plot of the observed intensity  $I_{obs}$  in observer's sky, in which the gray region represents the black hole shadow. Due to the redshift factor g, the observed intensity  $I_{obs}$  are not like the emitted specific intensity  $I_{em}$ , which arises from horizon, and increases from direct emission to lensing ring,

and reach peak in photon ring as L increases. Then it falls down as L continues to increase. The direct emission dominates a significant portion, constituting the major part in the black hole image. The lensing ring is much brighter than direct emission, forms a brilliant, glowing halo in black hole image. Although the photon ring exhibits the highest brightness, it is so narrow that its contribution can be ignored.

In the dynamical spacetime, the black hole shadow, direct emission, lensing ring and photon ring are also dynamic with time. The variations in the range of angular momentum L and R for the black hole shadow, direct emission, lensing ring and photon ring with the observer time  $t_o$  are shown in Fig. 9. And the observer is located at  $r_o = 50$ . The shadow range increases over time  $t_o$ . The range of direct emission is divided into two parts, and the entire range remains almost invariant with respect to  $t_o$ . The range of lensing ring is also divided into two parts, but the entire range decreases over  $t_o$ . While the range of photon ring is very narrow, and decreases over  $t_o$ .

Figure 10 shows the black hole images observed at  $t_o = 110,140$ , and 200 with  $r_o = 50$ . The upper row of this figure shows the images of black hole with an accretion disk. The gray inner region is the black hole shadow, whose radius increases as  $t_o$  increases, though the increase is very small. The shadow radius is approximately around 2.15. The bottom row of this figure illustrates black hole shadows without an accretion disk. The gray region is black hole shadow, which also become bigger with the increase of  $t_o$ . The colored region represents the image of the spherical background light source, consistent with the configuration described in Ref.[34]. The radius of the black hole shadow without an accretion disk is larger than that with an accretion disk, measuring approximately 3.95. Figure 11 illustrates the variations in the

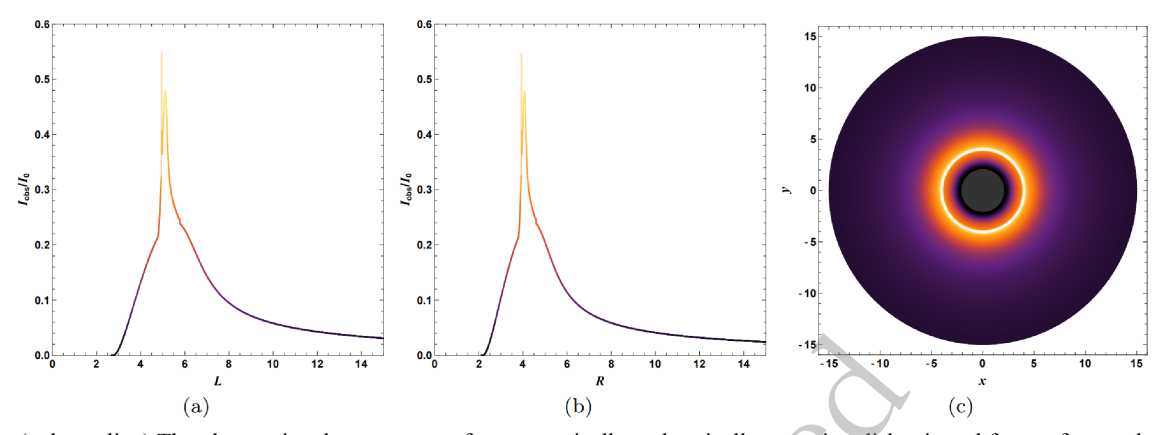


**Fig. 8.** (color online) The observational appearance of a geometrically and optically accretion disk, viewed from a face-on by the observer with radius  $r_o = 50$  and time  $t_o = 170$ . (a) The profiles of observed intensity  $I_{obs}$  as a function of the angular momentum L. (b) The profiles of observed intensity  $I_{obs}$  as a function of radial coordinate  $R = \sqrt{x^2 + y^2}$  in observer's sky. (c) The density plot of the observed intensity  $I_{obs}$  in black hole image, in which the gray region represents the black hole shadow.

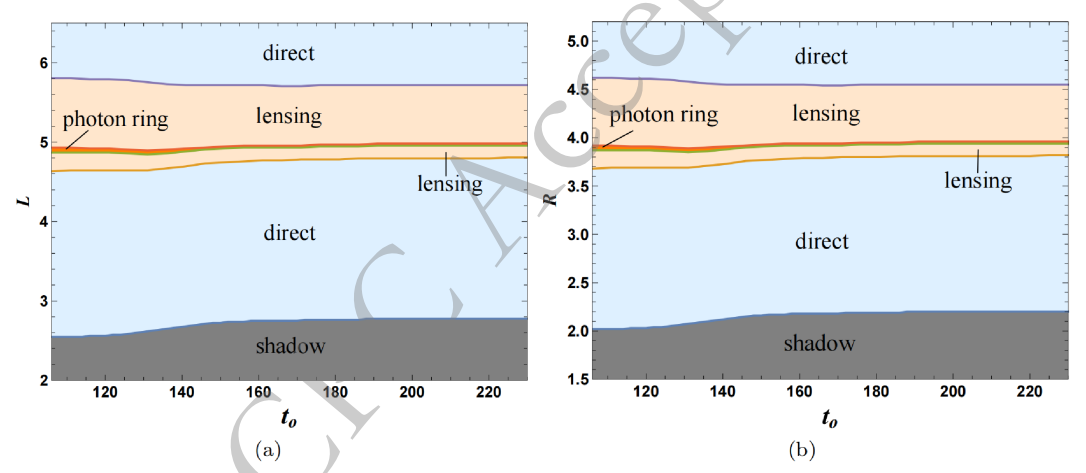
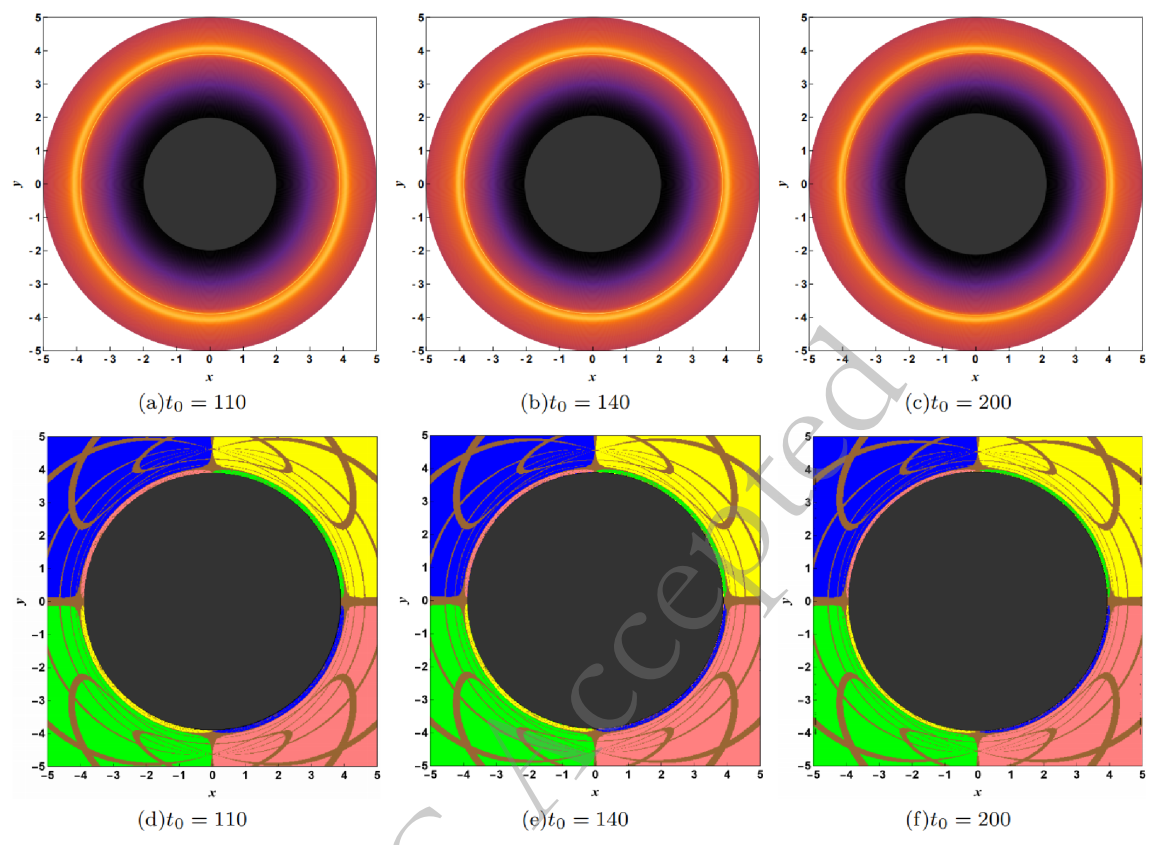


Fig. 9. (color online) The variations in the range of angular momentum L and R for the black hole shadow, direct emission, lensing ring, and photon ring with the observer time  $t_o$ . Here the observer is located at  $r_o = 50$ .

black hole shadow radius  $R_{sh}$  over observer time  $t_o$  for different observer distances  $r_o$ . Figure 11 (a) and (b) correspond to the black hole images with and without an accretion disk, respectively. In either case, the shadow radius  $R_{sh}$  of this dynamic black hole increases with observer time  $t_o$ . In the case with an accretion disk, the shadow radius  $R_{sh}$  increases as the observer distance  $r_o$  increases only when  $t_o$  is sufficiently large. In the absence of an accretion disk, the shadow radius  $R_{sh}$  is larger and increases as  $r_o$  increases. We did not start the observer time to from 0 because of the time delay for light rays to propagate from the light source to the observer. The light rays observed in the black hole image are emitted at different times from light sources. If  $t_0$  is too small, for some light rays (particularly those near the shadow), the backward-evolved time t might be less than 0. And times t < 0 are beyond the scope of our consideration. From Fig. 4, one can find the apparent horizon  $r_h$  and photon sphere  $r_{ps}$  approach an asymptotic stable state as the time t increases. Therefore, the variation of shadow radius  $R_{sh}$ 

with  $t_o$  in Fig. 10 and Fig. 11 are very small.

In order to investigate the characteristics of the black hole shadow at every time points, we slice the dynamical spacetime into spacelike hypersurfaces at different time t. At every spacelike hypersurface, the time t is fixed. We can study the black hole shadow in the spacelike hypersurface at any moment. Figure 12 exhibits the black hole shadows with t = 0, 10, and 100. The upper row shows the black hole images with an accretion disk, and the bottom row illustrates the black hole shadows without an accretion disk. It can be observed that the radius  $R_{sh}$  of black hole shadow increases as t increases. Moreover, the variation of shadow radius  $R_{sh}$  are much bigger than that in Fig. 10. The variations in the black hole shadow radius  $R_{sh}$  over time t for different  $r_o$  are illustrated in Fig. 13. Figure 13 (a) and (b) correspond to the black hole images with and without an accretion disk, respectively. For the case with an accretion disk, the black hole shadow radius  $R_{sh}$  has no change at the beginning of time t, then increases rapidly. As time t progresses, it exhibits a trend of



**Fig. 10.** (color online) The black hole shadows observed at  $t_o = 110,140$ , and 200 with  $r_o = 50$ . The upper row shows the images of black hole with an accretion disk. The bottom row illustrates the black hole shadow images without an accretion disk. The gray inner regions represent the black hole shadows.

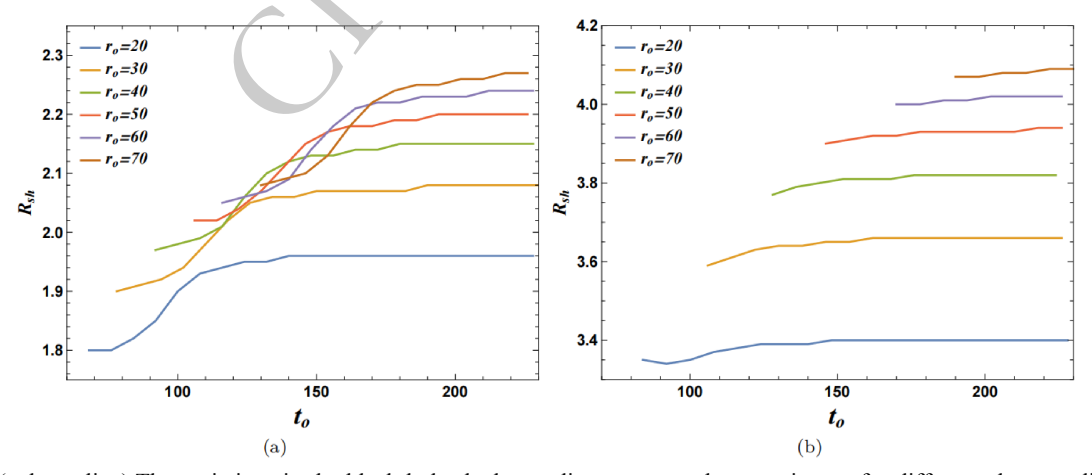


**Fig. 11.** (color online) The variations in the black hole shadow radius  $R_{sh}$  over observer time  $t_o$  for different observer distances  $r_o$ . (a) The shadow radius  $R_{sh}$  for this dynamic black hole with an accretion disk. (b) The shadow radius  $R_{sh}$  without an accretion disk.

gradual stabilization. In the absence of an accretion disk, the  $R_{sh}$  also has no change initially, then shows a significant increase. As time t increases, it undergoes damped oscillations before finally converging to a steady state. In either case, the  $R_{sh}$  is bigger for larger  $r_o$ . Compare with Fig. 4, it can be observed that the variation of  $R_{sh}$  for the case with an accretion disk is similar to that of the apparent horizon  $r_h$ , while the variation of  $R_{sh}$  for the case

without an accretion disk is similar to that of the photon sphere  $r_{ps}$ . It is because that the shadow boundary of black hole with an accretion disk is determined by the inner edge of the accretion disk, which extends to the apparent horizon. For the case without an accretion disk, the shadow boundary of a black hole is determined by the photon sphere. Since the variation of  $r_{ps}$  is induced by the change of the complex scalar field  $\psi$ , it can be stated that

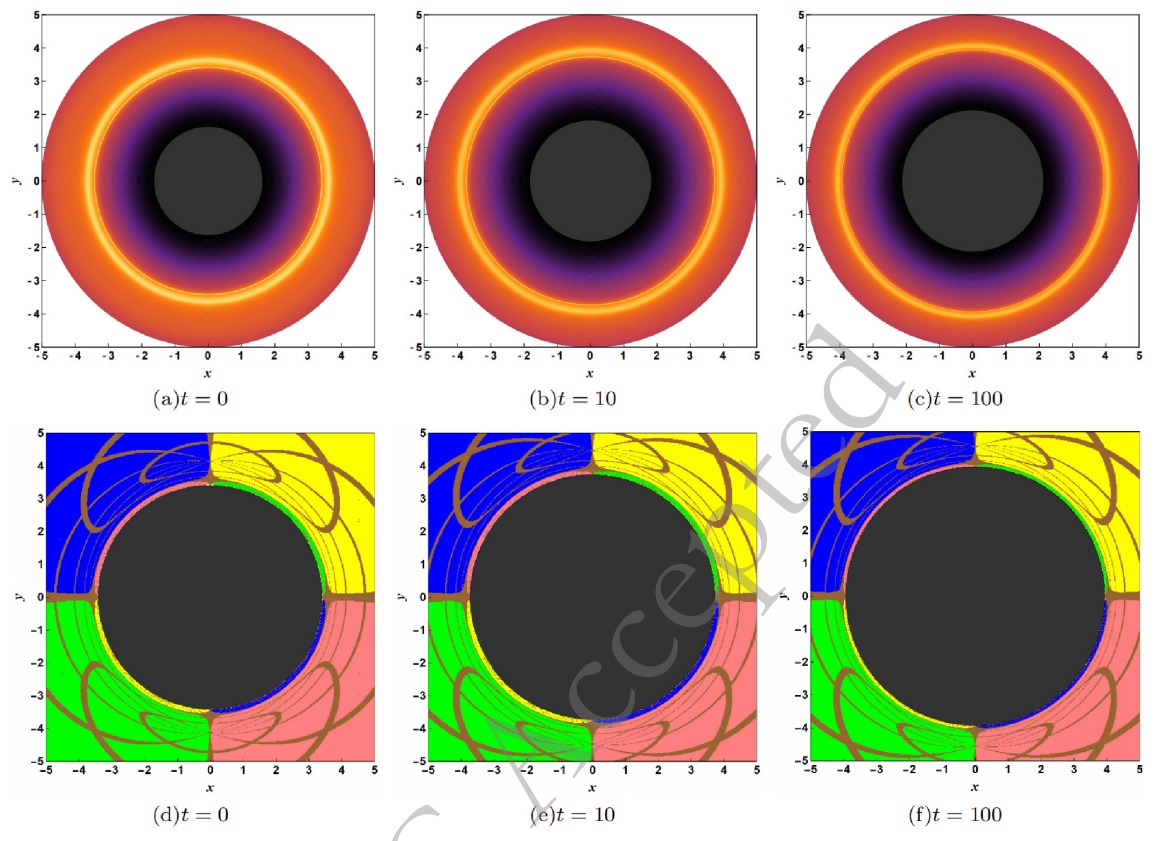
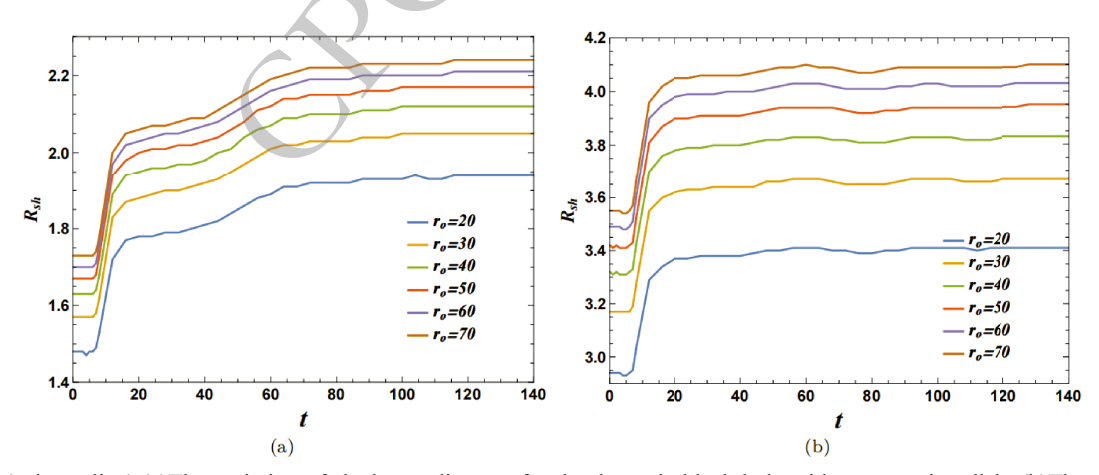


Fig. 12. (color online) The black hole images with and without an accretion disk when t = 0, 10, and 100. The upper row shows the images of the black hole with an accretion disk. The bottom row illustrates the black hole shadow images without an accretion disk.



**Fig. 13.** (color online) (a) The variation of shadow radius  $R_{sh}$  for the dynamic black hole with an accretion disk. (b) The variation of shadow radius  $R_{sh}$  for the dynamic black hole without an accretion disk.

the variation in the size of the shadow is likewise caused by the change of  $\psi$ . Furthermore, regardless of the presence or absence of the accretion disk, the emergence of the complex scalar hair  $\psi$  causes the radius  $R_{sh}$  of the shadow to start changing.

Since the spacetime of black hole with a self-interacting massive complex scalar hair is dynamical, it is essential to investigate the time delay of light rays in the black hole image. Figure 14 shows the time delay  $\Delta t = t_o - t_e$  of

lights propagating from accretion disk to observer. Here, the observer time  $t_o = 170$ , and the radius coordinate of the observer  $r_o = 50$ . Figure 14 (a) and (b) exhibit the variation of time delay  $\Delta t$  with angular momentum L and the radius R on the observer's screen, respectively. Blue, orange and red lines represent the time delay  $\Delta t$  of lights from direct emission, lensing ring and photon ring, respectively. On average, the time delay  $\Delta t$  of light rays from the photon ring is the largest, followed by that from

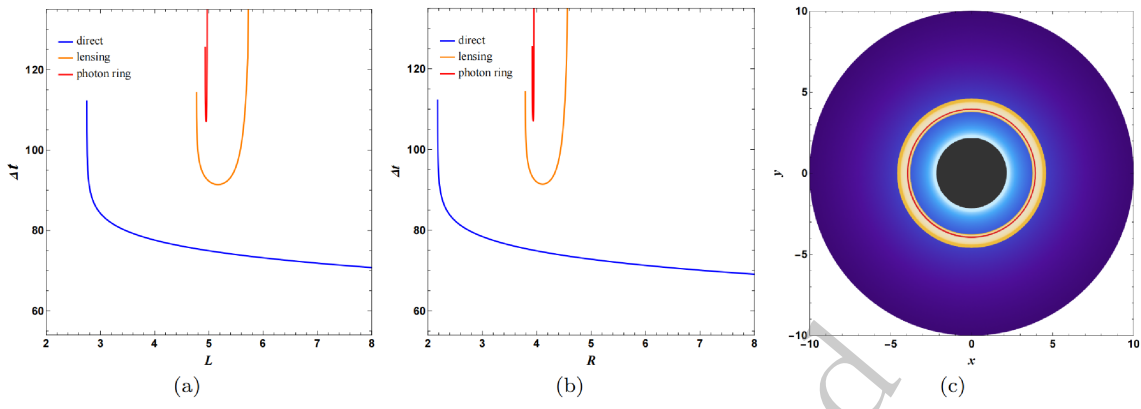


**Fig. 14.** (color online) The time delay  $\Delta t = t_o - t_s$  of lights propagating from accretion disk to observer. (a)The variation of time delay  $\Delta t$  with angular momentum L. (b)The variation of time delay  $\Delta t$  with the radius R on the observer's screen. (c)The density plot of the time delay  $\Delta t$  of lights in black hole image, in which the gray inner region represents the black hole shadow.

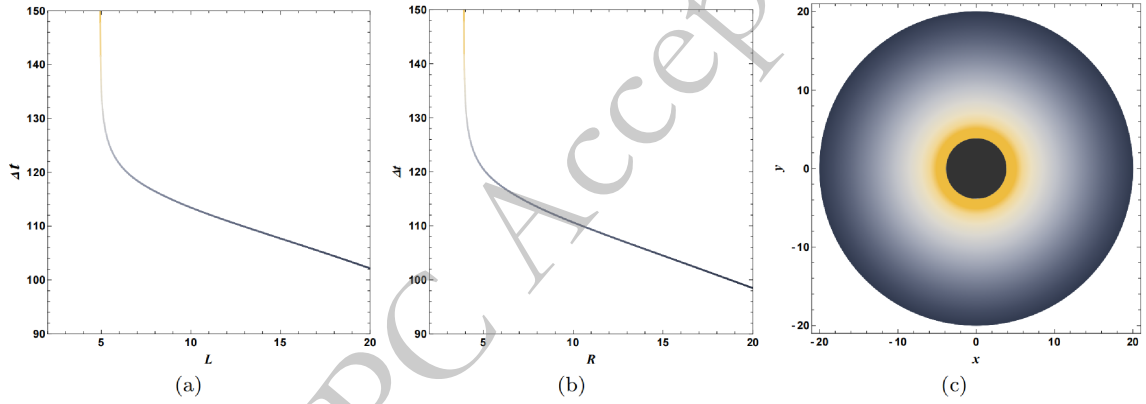


**Fig. 15.** (color online) The time delay  $\Delta t = t_0 - t_s$  of lights propagating from a spherical background light source to observer. (a) The variation of time delay  $\Delta t$  with angular momentum L. (b) The variation of time delay  $\Delta t$  with the radius R on the observer's screen. (c) The density plot of the time delay  $\Delta t$  of lights in black hole image, in which the gray inner region represents the black hole shadow.

the lensing ring, and the smallest is that from the direct emission. The time delay  $\Delta t$  in the direct emission decreases with the increase of L and R. The time delay  $\Delta t$  in the lensing ring and photon ring first decreases and then increases as L or R increases. It is because the light rays with small L originate from the accretion disk close to the horizon and are subject to stronger gravity. The light rays with large L originate from the exterior of the accretion disk and require more time to traverse longer trajectories. Figure 14 (c) exhibits the density plot of the time delay  $\Delta t$  of lights in black hole image, in which the gray inner region represents the black hole shadow.

In the case of no accretion disk, lights propagate from a spherical background light source with radius  $r_s = 50$  to observer. Figure 15 illustrates the time delay  $\Delta t = t_o - t_s$  of lights propagating from the light source to observer. Here, the observer is located at  $r_o = 50$ , and the observer time  $t_o = 170$ . Figure 15 (a) and (b) exhibit the variation of time delay  $\Delta t$  with angular momentum L and the radius R on the observer's screen, respectively. Initially, when L is small, the time delay  $\Delta t$  approaches infinity because the corresponding light rays spiral asymptotically toward

the photon sphere, where they can orbit the black hole multiple times. And then the time delay  $\Delta t$  decreases as L or R increases. Figure 15 (c) exhibits the density plot of the time delay  $\Delta t$  of lights in black hole image, in which the gray inner region represents the black hole shadow.

# IV. CONCLUSION

In this work, we research dynamic shadows of a black hole with a self-interacting massive complex scalar hair. We first provide a brief review of the spacetime of the dynamic black hole. The complex scalar field  $\psi$  evolves with time t. At the initial time t, the magnitude of the complex scalar field on the horizon is given by  $|\psi_h| = 0$ , indicating that the black hole has not yet acquired scalar hair. Subsequently,  $|\psi_h|$  exhibits a sharp rise, followed by rapid oscillations, and finally converges to a stable value. Affected by the complex scalar field  $\psi$ , the variation of the photon sphere radius  $r_{ps}$  is similar to that of the magnitude  $|\psi_h|$ . The emergence of the complex scalar hair  $\psi$  causes the apparent horizon radius  $r_h$  to start increasing sharply, and smoothly approaches a stable value eventu-

ally. Then, we research the direct emission, lensing ring and photon ring of a faced-on thin disk in the dynamical spacetime. We calculated the specific intensity of light rays received by the observer from an accretion disk, and exhibit the observational appearance of the dynamic black hole shadow. For the case with an accretion disk, the black hole shadow radius  $R_{sh}$  increases with the observer time  $t_o$ . The ranges of the lensing ring and photon ring decrease with  $t_o$ , and the range of the direct image remains almost invariant with  $t_o$ . In the absence of an accretion disk, the shadow radius  $R_{sh}$  is larger and also increases as  $t_o$  increases.

Furthermore, we slice the dynamical spacetime into spacelike hypersurfaces to investigate the black hole shadow for all time points  $(t \ge 0)$ . For the case with an accretion disk, the variation of  $R_{sh}$  is similar to that of the apparent horizon  $r_h$ , because the inner edge of the accretion disk extends to the apparent horizon. In the absence of an accretion disk, the variation of  $R_{sh}$  is similar to that of the photon sphere  $r_{ps}$ , because the black hole shadow boundary is determined by photon sphere. Since the variation of  $r_{ps}$  is induced by the complex scalar field  $\psi$ , it

can be stated that the variation in the size of the shadow is likewise caused by the change of  $\psi$ . In addition, regardless of the presence or absence of the accretion disk, the emergence of the complex scalar hair  $\psi$  causes the radius  $R_{sh}$  of the shadow to start changing.

In the dynamical spacetime of a black hole with a self-interacting massive complex scalar hair, we investigate the time delay  $\Delta t = t_o - t_e$  of lights propagating from light sources to observer. The time delay  $\Delta t$  in the direct emission from accretion disk decreases with the increase of L or R. The time delay  $\Delta t$  in the lensing ring and photon ring first decreases and then increases as L or R increases. Without an accretion disk, we set a spherical background light source with  $r_s = 50$ . The time delay  $\Delta t$  decreases from infinity as L or R increases.

This paper demonstrates the characteristics in dynamic black hole shadows between scenarios with and without an accretion disk. These findings not only enrich the theoretical models of dynamic black hole shadows but also provide a significant reference value in the research of observational astronomy and theoretical physics on black hole images.

## References

- [1] The Event Horizon Telescope Collaboration, Astrophys. J. Lett. **875**, L1 (2019)
- [2] The Event Horizon Telescope Collaboration, *et al.*, Astrophys. J. Lett. **930**, L12 (2022)
- [3] J. L. Synge, Mon. Not. Roy. Astron. Soc. 131, 463 (1966)
- [4] J. M. Bardeen, Timelike and null geodesics in the Kerr metric, in Black Holes (Les Astres Occlus), edited by C. DeWitt and B. DeWitt (Gordon and Breach, New York, 1973), p. 215-239.
- [5] J. P. Luminet, Astron. Astrophys. **75**, 228 (1979)
- [6] S. Chandrasekhar, The Mathematical Theory of Black Holes (Oxford University Press, New York, 1992).
- [7] K. Hioki, K. I. Maeda, Phys. Rev. D **80**, 024042 (2009)
- [8] Z. Li, C. Bambi, J. Cosmol. Astropart. Phys. 1401, 041 (2014)
- [9] L. Yang, Z. Li, Int. J. Mod. Phys. D 25, 2 1650026 (2016).
- [10] S. Wei, Y. Liu, R. B. Mann, Phys. Rev. D 99, 041303 (2019)
- [11] R. Kumar, S. G. Ghosh, Astrophys. J 892, 78 (2020)
- [12] Z. Chang, Q. Zhu, J. Cosmol. Astropart. Phys. 09, 003 (2021)
- [13] S. Wei, Y. Zou, arXiv: 2108.02415v1.
- [14] X. Hou, Z. Xu, M. Zhou, et al., J. Cosmol. Astropart. Phys. 07, 015 (2018)
- [15] R. A. Konoplya, Phys. Lett. B **795**, 1 (2019)
- [16] K. Jusufi, M. Jamil, P. Salucci, et al., Phys. Rev. D 100, 044012 (2019)
- [17] M. Jamil, K. Jusufi, K. Lin, et al., Phys. Rev. D 99, 044015 (2019)
- [18] K. Jusufi, M. Jamil, T. Zhu, Eur. Phys. J. C 80, 354 (2020)
- [19] L. Amarilla, E. F. Eiroa, G. Giribet, Phys. Rev. D 81, 124045 (2010)
- [20] S. Dastan, R. Saffari, S. Soroushfar, Eur. Phys. J. Plus 137,

- 1002 (2022)
- [21] R. Kumara, B. P. Singha, S. G. Ghosh, Annals Phys. 420, 168252 (2020)
- [22] F. Long, S. B. Chen, M. Z. Wang, et al., Eur. Phys. J. C 80, 1180 (2020)
- [23] A. Stepanian, Sh. Khlghatyan, V.G. Gurzadyan, Eur. Phys. J. Plus 136, 127 (2021)
- [24] V. Prokopov, S. Alexeyev, O. Zenin, J. Exp. Theor. Phys. 135, 91 (2022)
- [25] Z. Younsi, D. Psaltis, F. Özel, Apj 942, 47 (2023).
- [26] J. L. Jing, S. Long, W. K. Deng, et al., Phys. Mech. Astron. 65, 100411 (2022)
- [27] J. L. Jing, S. Chen, M. M Sun, et al., Phys. Mech. Astron. 65, 260411 (2022)
- [28] J. L. Jing, W. K. Deng, S. Long, et al., Phys. Mech. Astron. 66, 270411 (2023)
- [29] Y. H. Zou, M. J. Wang, J. L Jing, Sci. China, Phys. Mech. Astron. 64, 250411 (2021)
- [30] W. T. Liu, X. J Fang, J. L. Jing, et al., Phys. Mech. Astron. 66, 210411 (2023)
- [31] X. Zhou, S. B. Chen, J. L. Jing, Sci. China, Phys. Mech. Astron. 65, 250411 (2022)
- [32] L. OuYang, D. Wang, X. Y. Qiao, et al., Phys. Mech. Astron. 64, 240411 (2021)
- [33] M. Z. Wang, S. B. Chen, J. L. Jing, Eur. Phys. J. C 81, 509 (2021)
- [34] M. Z. Wang, S. B. Chen, J. L. Jing, Phys. Rev. D 98, 104040 (2018)
- [35] M. Z. Wang, S. B. Chen, J. L. Jing, J. Cosmol. Astropart. Phys. 10, 051 (2017)
- [36] M. Z. Wang, S. B. Chen, J. L. Jing, Phys. Rev. D 104, 084021 (2021), arXiv:2104.12304v2.
- [37] M. Z. Wang, S. B. Chen, J. C. Wang, et al., Eur. Phys. J. C 80, 110 (2020)
- [38] M. Z. Wang, S. B. Chen, J. L. Jing, Phys. Rev. D 97,

#### 064029 (2018)

- [39] M. Z. Wang, G. H. Guo, S. B. Chen, et al., Chinese Physics C 47, 1 (2023)
- [40] S. B. Chen, M. Z. Wang, J. L. Jing, JHEP **07**, 054 (2020)
- [41] M. Z. Wang, S. B. Chen, J. L. Jing, Commun. Theor. Phys. 74, 097401 (2022)
- [42] P. V. P. Cunha, C. A. R. Herdeiro, E. Radu, et al., Phys. Rev. Lett. 115, 211102 (2015)
- [43] P. V. P. Cunha, C. A. R. Herdeiro, E. Radu, et al., Int. J. Mod. Phys. D 25, 1641021 (2016)
- [44] F. H. Vincent, E. Gourgoulhon, C. A. R. Herdeiro, et al., Phys. Rev. D 94, 084045 (2016)
- [45] P. V. P. Cunha, J. Grover, C. A. R. Herdeiro, et al., Phys. Rev. D 94, 104023 (2016)
- [46] T. Johannsen, Astrophys. J. 777, 170 (2013)
- [47] M. Z. Wang, S. B. Chen, J. L. Jing, Sci. China, Phys. Mech. Astron. 66, 110411 (2023)
- [48] P. V. P. Cunha, C. A. R. Herdeiro, E. Radu, Phys. Rev. D 96, 024039 (2017)
- [49] S. W. Wei, Y. C. Zou, Y. X. Liu, et al., J. Cosmol. Astropart. Phys. 08, 030 (2019)

- [50] F. Long, J. C. Wang, S. B. Chen, et al., JHEP 10, 269 (2019)
- [51] J. Grover, A. Wittig, Phys. Rev. D **96**, 024045 (2017)
- [52] Z. L. Zhang, S. B. Chen, X. Qin, et al., Eur. Phys. J. C 81, 991 (2021)
- [53] X. Qin, S. B. Chen, J. L. Jing, Eur. Phys. J. C 82, 784 (2022)
- [54] X. Y. Liu, S. B. Chen, J. L. Jing, Sci. China, Phys. Mech. Astron. 65, 120411 (2022)
- [55] Z. L. Zhang, S. B. Chen, J. L. Jing, Eur. Phys. J. C 82, 835 (2022)
- [56] S. B. Chen, J. L. Jing, W. L. Qian, et al., Phys. Mech. Astron. 66, 260401 (2023)
- [57] X. Qin, S. B. Chen, Z. L. Zhang, et al., Eur. Phys. J. C 83, 159 (2023)
- [58] Y. P. Zhang, S. W. Wei, Y. X. Liu, arXiv: 2503.14159v1.
- [59] C. Y. Zhang, Q. Chen, Y. X Liu, *et al*, arXiv: 2309.05045v2.
- [60] K. Beckwith, C. Done, MNRAS **359**, 1217 (2005)
- [61] S. E. Gralla, D. E. Holz, R. M. Wald, Phys. Rev. D 100, 024018 (2019)